Inorganic Chemistry

pubs.acs.org/IC
Article

Two P, Ten P, White P, Red P: Mechanistic Exploration of the Oligomerization of Red Phosphorus from Diphosphorus with the Ab Initio Nanoreactor

Nathan D. Yoshino* and Lee-Ping Wang*

Cite This: *Inorg. Chem.* 2024, 63, 19074−19086
Read Online

ACCESS | Metrics & More | Article Recommendations | Supporting Information

ABSTRACT: Phosphorus is critical to humans on many fronts, yet we do not have a mechanistic understanding of some of its most basic transformations and reactions—namely the oligomerization of white phosphorus to red. With heat or under ultraviolet (UV) exposure, it has been experimentally demonstrated that white phosphorus dissociates into diphosphorus units which readily form red phosphorus. However, the mechanism of this process is unknown. The ab initio nanoreactor approach was used to explore the potential energy surface of phosphorus clusters. Density functional theory and metadynamics simulations were used to characterize potential reaction pathways. A mechanism for oligomerization is proposed to take place via diphosphorus additions at π-bonds and weak σ-bonds through three membered ring intermediates. Downhill paths through P_6 and P_8 clusters eventually result in P_{10} clusters that can oligomerize into red phosphorus chains. The initial, rate limiting step for this process has an energy barrier of 24.2 kcal/mol.

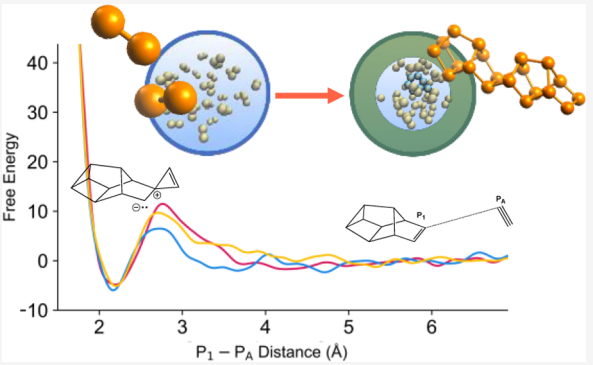

INTRODUCTION

Phosphorus (P) is an essential element in the genetic code and cellular metabolism,[1] as well as many industrially produced materials and organic compounds such as pharmaceuticals, foodstuffs,[2] semiconductors (e.g., gallium phosphide)[3] and fertilizer.[4] With this many applications, an optimal process for producing elemental phosphorus is necessary. Elemental phosphorus is classified into three allotropes:

1. White phosphorus—tetrahedral P_4 with a low melting point (44.15 °C)[5]
2. Black phosphorus—stacked 2D honeycomb lattice similar to graphite[6]
3. Red phosphorus—many forms with varying levels of structure[7]

Current industrial phosphorus generation uses a thermal process to convert phosphates into white P and subsequently phosphorus trichloride[2] as a feedstock for other compounds, but this requires large amounts of energy and uses hazardous chlorine gas.

Alternative methods of more direct phosphorus generation are of great interest in order to omit chlorine from the process.[8−14] Experimental research efforts led by Cummins et al. have included ultraviolet (UV) photolysis of P_4 to incorporate diphosphorus (P_2) units directly into synthetic schemes.[15] This work is inspired by the observation that P_4 oligomerization to red P can be initiated by photolysis of P_4 into P_2 units under UV light[16] (Figure 1) or at high temperatures (>275 °C).[2,7,17,18] Red P is known to exist in at least five forms from amorphous[7] (form I) to the well-defined tubular structure of fibrous red phosphorus[19] (form IV) and Hittorf's violet phosphorus (form V).[20,21] Changes between forms are induced at high temperatures (>450 °C) and are irreversible.[7]

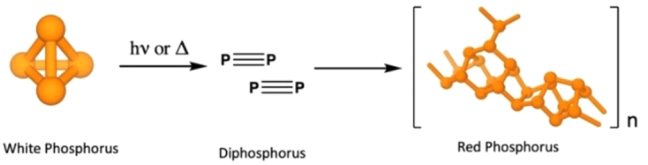

Figure 1. White phosphorus dissociates to P_2, which oligomerizes to red phosphorus. Some red phosphorus forms contain repeated P_{10} and P_{11} subunits. P_{11} subunits in different chains cross-link to form an extended network.

Red phosphorus itself has compelling, unexplored potential. Historically, its main uses are in flame retardants and

Received: June 3, 2024
Revised: September 11, 2024
Accepted: September 17, 2024
Published: October 1, 2024

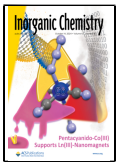

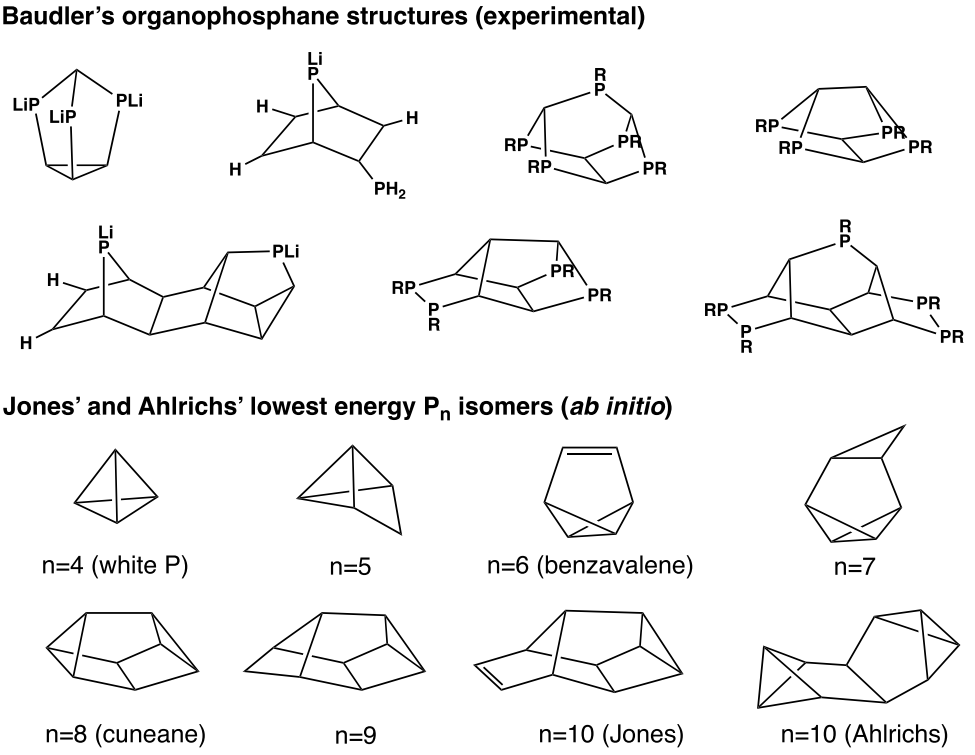

Figure 2. Previously studied phosphorus clusters by Baudler, Jones, and Ahlrichs.

matchboxes.[22] However, there is a great body of work suggests Red P will play a key role in sustainable energy.[23,24] Initial efforts by Wang et al.[25] with Red P microparticles demonstrated high levels of hydrogen gas evolution for an elemental photocatalyst. Compared to its metal-based counterparts, Red P has several advantages such as stability, nontoxicity, and cost. Many other studies have confirmed the photocatalytic hydrogen evolution potential of Red P in other forms or when combined with other photocatalysts.[26−39] In addition, Red P's photocatalytic use could extend to pollutant degradation[40−43] and bacterial inactivation to clean water.[43−45] Recent work has also shown Red Phosphorus to be useful for energy storage as a candidate for use in anodes of ion batteries. Carbon/Red P materials have been extensively studied and demonstrated areal capacities of up to 10 mA h cm^{2-},[46] boosted ion storage and good stability.[46−55]

The reaction pathways of red P formation from P_2 may involve traversing a landscape of oligophosphorus and polyphosphorus molecules. Clues are provided in the rich chemistry of organophosphane compounds, in which a great number of P_n-containing structural motifs were described by Baudler,[56] Weigand,[57,58] Hey-Hawkins,[59] and others. Some of these compounds have versatile metal coordination capabilities,[60−65] and may be used as precursors to metal phosphides,[59,66] which are challenging to synthesize but have potential to replace precious metal catalysts in reactions such as hydrogen evolution. Therefore, studies of P_n cluster growth of intermediate cluster sizes could further guide the discovery of novel polyphosphorus compounds and derived functional materials.

The first to speculate on the structure of Red P and phosphorus clusters was Pauling, who initially proposed a structural model of red P based on X-ray analysis[6] consisting of linked units of tetrahedral white P with one bond broken.[67] The structure of Hittorf's phosphorus was later characterized by Thurn and Krebs,[20] followed by the discovery of similar structural motifs in amorphous red P by Fasol et al.[21] Subsequently, Baudler characterized a vast array of monocyclic and polycyclic phosphanes (Figure 2). The vertices of all skeletal structures from here on will indicate a phosphorus atom unless otherwise specified., showing that the parallel, tubular structure of red P could be synthesized from nucleophilic additions of compounds containing P_2 and P_4 subunits.[68−73] These studies generally observed that organophosphorus clusters will maximize the number of five-membered rings formed while avoiding four and seven-membered rings; three-membered rings are also more thermally stable than six-membered rings.[56]

While experimental isolation of small elemental P clusters has not yet been achieved, mass spectroscopy (MS) has provided some insights. Early work by Kerwin[74,75] using electron ionization MS suggested that P_n clusters, n = 2−4 (particularly P_4) dominate red P vapors at temperatures from 100−300 °C, along with trace amounts of P_8.[76,77] This was followed by discovery of larger clusters including up to P_{24} in red P vapor[78] and up to P_{89} in laser desorption ionization experiments.[79−82]

In the past few decades, small P clusters have been extensively characterized with theoretical methods. Early studies[83−85] found repulsive interactions between parallel P−P bonds in four-membered rings, consistent with experimental observations disfavoring these structures.[56] Ahlrichs et al. studied the most stable even-numbered isomers of P_n clusters up to n = 28 with the Hartree−Fock (HF) and MP2 methods[86] and hypothesized that these structures were intermediates in red P formation. Concurrently, Jones et al.[87−89] carried out density functional theory (DFT) studies for neutral and ionic P clusters up to n = 11. Both studies largely agreed on the most stable structures of P clusters with one exception being P_{10} (Figure 2)—Jones' structure was later favored by more accurate CCSD(T) calculations by Häser.[53] These initial studies, together with neutron diffraction experiments[90] suggest that amorphous red P contains cuneane-like P_8 clusters reminiscent of the tubular

https://doi.org/10.1021/acs.inorgchem.4c02299
Inorg. Chem. 2024, 63, 19074−19086

structure of Hittorf's (form V) and fibrous (form IV) red P. Häser's theoretical studies[73,91,92] revealed the following trends: P_n clusters with $n \geq 10$ are more stable relative to P_4 and those with $n = 6-8$ are less stable. Islands of stability do not exist beyond $n = 4$, but stability gradually increases with cluster size due to increasing the number of strain-free five-membered rings.[73] Gimarc and Warren's exploration[93−95] of strain energies in P clusters affirms this, estimating cuneane P_8 as having the smallest ring strain for P_8 isomers. DFT studies on ionic P clusters revealed similar cuneane-like structural motifs and noted that odd-numbered clusters were more stable than even-numbered ones.[80,96−99] New families of stable ionic cluster structures were found using DFT simulated annealing, suggesting that broad exploration of the potential energy surface is useful for finding new isomers.[100]

With the abundance of experimental and theoretical investigations of organophosphanes and P clusters, their structural patterns and the factors that contribute to their stabilities are well understood. However, the chemical transformations between these species have not been thoroughly explored. While Häser and Ahlrichs have proposed mechanisms for the oligomerization of red P,[86] their analyses were based solely on energetic minima of phosphorus clusters on the PES and did not examine the kinetic feasibility of the proposed pathways. It is the purpose of this work to propose a kinetically reasonable mechanism for the oligomerization of red P by characterizing the reaction network that connect small phosphorus clusters of varying size.

Many mechanistic investigations start with informed hypotheses from known reactions or by chemical intuition, but the reactivity of elemental P has a much smaller body of experimental knowledge and the derived chemical intuition is also greatly reduced. Moreover, Jones[87,88] and Xue[100] previously demonstrated with their simulated annealing studies that computational methods that reduce bias and the need for guesswork are highly useful for improved understanding of these systems. The recent decade has seen the development of many methods for automatic generation and characterization of reaction pathways, including those based on the automated application of elementary reaction rules,[101−106] and molecular dynamics (MD) simulations on reactive potential energy surfaces.[107−111] Ab initio quantum chemistry and DFT are the most reliable methods for discovering previously unknown reactivity as they have the least amount of empirical fitting but are computationally very expensive. To mitigate this, ab initio molecular dynamics (AIMD)-based reaction discovery methods employ various methods to increase the frequency of reaction events relative to ambient conditions. Within this class of approaches, the ab initio nanoreactor[112] is an attractive option for simulating red P oligomerization, as it accelerates reactivity by inducing molecular collisions without relying on user-specified collective variables and can generate new hypotheses outside of any mechanistic space determined by rules. For these reasons the nanoreactor was chosen as the primary reaction discovery approach for this study.

Herein, we will first discuss how the ab initio nanoreactor was used to generate novel mechanistic hypotheses for the oligomerization of red P. Our initial simulations found P_2 oligomerization reactions that result in many of the stable isomers discussed above (Figure 3 and Table S1). We observed that diphosphorus units tend to add to existing phosphorus clusters via pseudopericyclic reactions to form three-member rings at π-bonds and weak σ-bonds, and we propose that this is a key step in the formation of red P. The reaction network results in forming Jones' P_{10} units which then oligomerize through the π-bonds at the bridging P atoms. Our work shows for the first time a detailed, mechanistic exploration of the P cluster reaction space and demonstrates that ab initio molecular dynamics can facilitate reaction discovery in chemical spaces that are largely unintuitive.

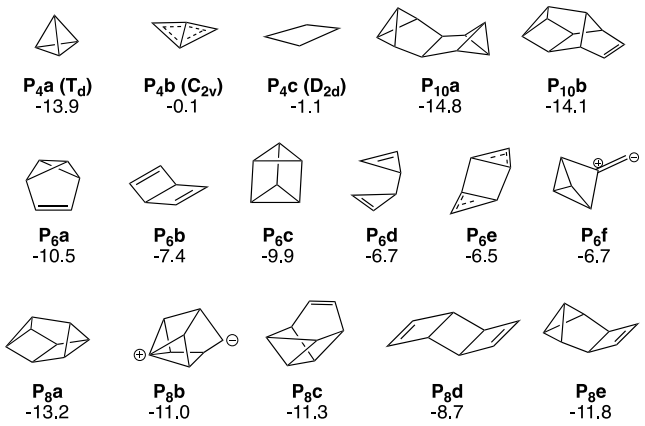

Figure 3. Small phosphorus clusters (P_2-P_{10}) observed in initial nanoreactor simulations with their per-atom energy (kcal/mol) relative to diphosphorus.

RESULTS AND DISCUSSION

From over 90 nanoreactor simulations, a large set of reaction pathways were characterized. Reactions that are perhaps most significant to a mechanism or were observed multiple times in simulations are summarized in Scheme 1. The numbers given are the electronic activation energy followed by the reaction energy in kcal/mol. Reactions without bold arrows were directly observed in the nanoreactor or during the path refinement process. Reactions with bolded arrows were inspired by nanoreactor results and modeled separately. Reactions stated as "<1.0" were calculated to be barrierless association reactions with our methods. It is notable that there are multiple pathways that lead toward cuneane P_8 and C_s P_{10} (Jones's P_{10}), which are fundamental building blocks for red P chains. Many of these pathways do not have particularly high barriers considering the temperatures that oligomerization occurs.

As amorphous forms of red P contain many structural motifs from forms V (Hittorf's) and IV,[90] we suggest that diphosphorus could follow the pathways in Scheme 1 as it oligomerizes into cuneane structures (Figure 4). Particularly the pathway (blue) starting from P_4c through to P_6b seems plausible. Even if P_6b isomerizes into P_6a—the most stable P_6 isomer—through ***reactions r*** and ***t***, there is still a downhill path (pink) to cuneane P_8 via a P_2 addition at the π-bond. P_6b will also readily react with any diphosphorus nearby (***reaction c***) minimizing the isomerization to P_6a. If P_4b is formed, it can react with another diphosphorus in two ways, forming P_6a through ***reaction o*** or P_6f through ***reaction j*** (gold) depending on the orientation of diphosphorus. ***Reaction o*** is likely preferred as it leads to the most stable P_6a isomer. The gold pathway through P_6f also contains P_6d which was by far the most common P_6 isomer observed in nanoreactor simulations. All three pathways seem plausible to form P_8a, and phosphorus clusters may isomerize between these paths as they traverse the potential energy surface downward toward the cuneane subunit of Red P.

https://doi.org/10.1021/acs.inorgchem.4c02299
Inorg. Chem. 2024, 63, 19074−19086

Scheme 1. Reactions Discovered in and Inspired by the Nanoreactor Simulations

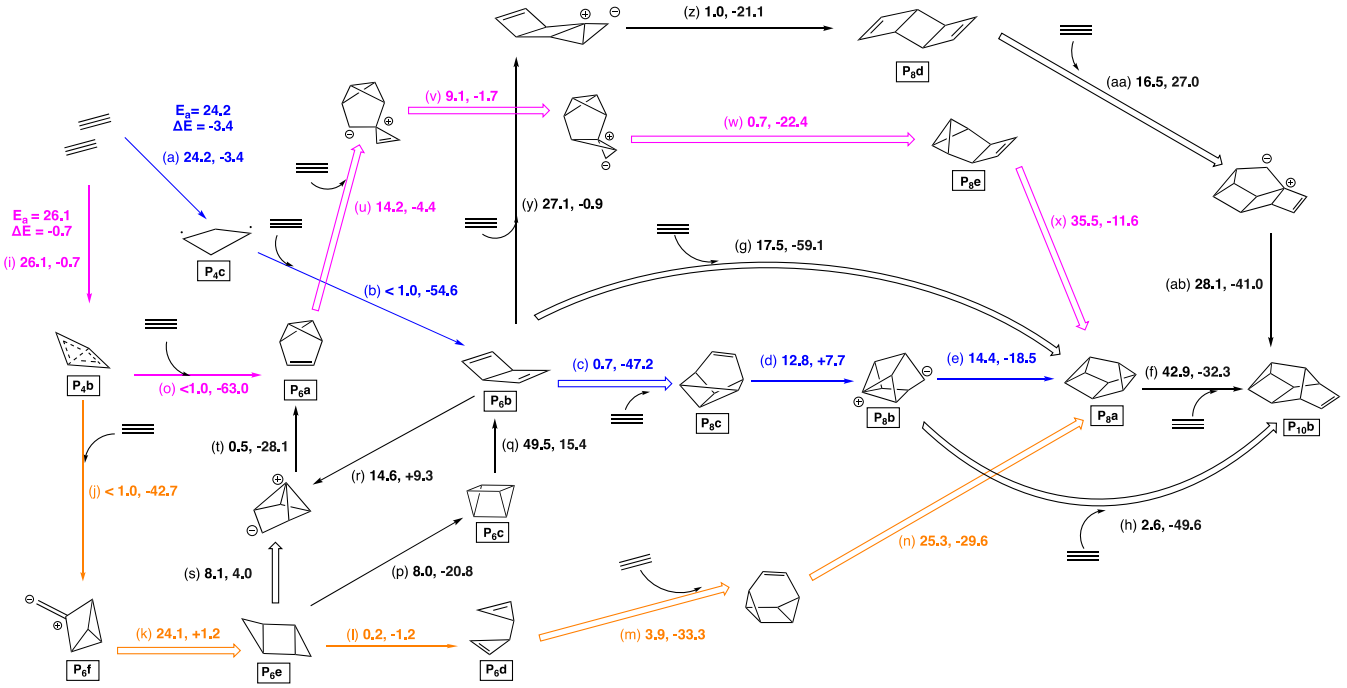

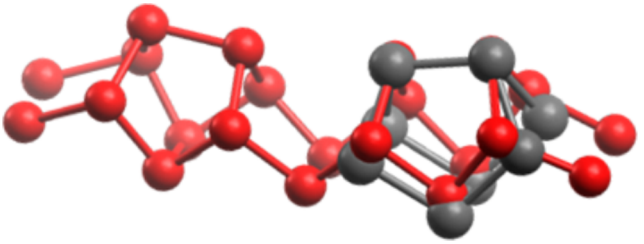

Figure 4. Optimized geometry of the main product (P_8a) from Scheme 1 (gray) corresponds to one subunit of Red P (red).

With these pathways characterized, we are also able to verify our choice of methods with previous work. In particular, in comparison to ref 113, which calculated the relative energies of several P_4 energy minima and the energy barriers between them using third order Rayleigh−Schrödinger perturbation theory (CASSCF-RSPT3 (4,9)) and an aug-cc-pVTZ basis set, our ωB97X-D3/def-TZVP calculations agree to within 0.2 eV for the activation energy for $2P_2 \rightarrow P_4$c (Figure S1) and the reaction energy of $2P_2 \rightarrow P_4$a (Table S2), and moderate agreement is found for the relative energies of other P_4 clusters (to within 0.5 eV). We think the smallest clusters are the most problematic for DFT due to the open-shell character of P_4b and P_4c and the breaking of multiple bonds in their reaction pathways;[114] these phenomena were not observed for the larger clusters in this study.

Pseudopericyclic P_2 Addition at π-Bonds. Addition of diphosphorus units through pseudopericyclic reactions emerged as a common motif in the nanoreactor simulations (Scheme 2). Scheme 2a shows a sterically strained three-membered ring intermediate but is the most energetically effective way to add a P_2 to the π-bond in P_{10}b whereas Scheme 2b corresponds to a [2 + 2] cycloaddition. Following Woodward−Hoffmann rules, the

Scheme 2. Reactions that Result from P_2 Addition to Jones' P_{10}[a]

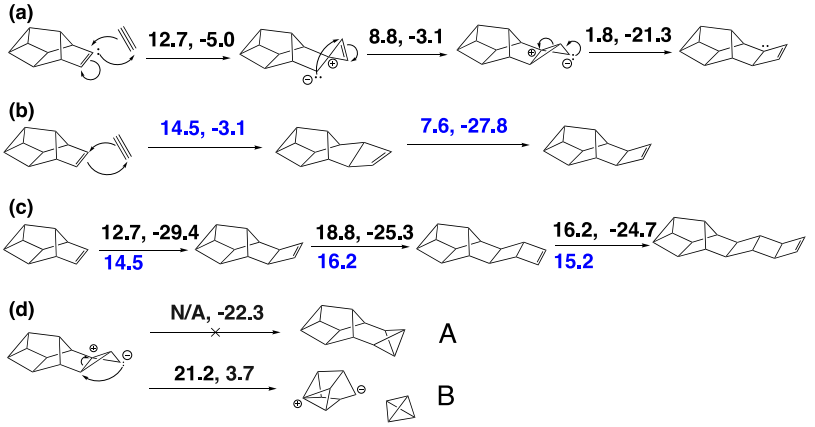

[a](a) Pseudopericyclic addition of P_2 at a π-bond. (b) [2 + 2] supra/antara cycloaddition of P_2 at a π-bond. (c) Comparison of [2 + 2] and pseudopericyclic addition of subsequent P_2. (d) Third structure in (a) cannot form bicyclic product.

https://doi.org/10.1021/acs.inorgchem.4c02299
Inorg. Chem. 2024, 63, 19074−19086

cycloaddition forces the newly formed ring into a supra/antara conformation that must undergo a phosphorus inversion to reach the same product. Relevant molecular orbitals (MO's) for the pseudopericyclic addition of diphosphorus is shown in Figure 5. Three MO's with distinct π-bond character are visible

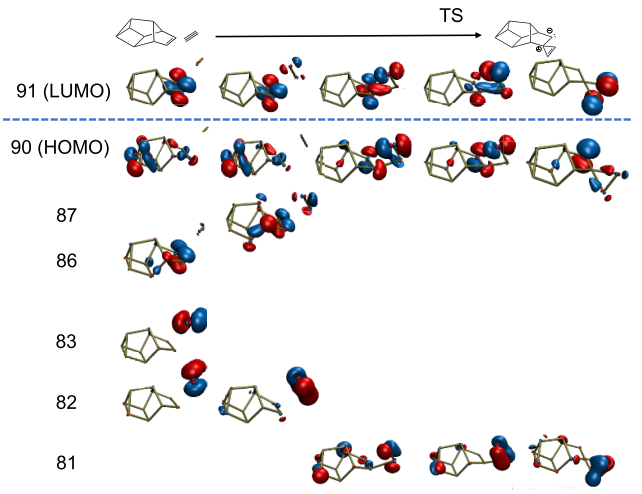

Figure 5. Relevant molecular orbitals for the pseudopericyclic addition of diphosphorus to Jone's P_{10}, following Scheme 2a.

in the reactant (MO 82, 83 and 86). One π-bond (82 → 81) stays consistent throughout the reaction coordinate. The π-bond character of the other P_2 π-bond and the P_{10} π-bond start to disappear during the association (87). During the association, the highest occupied molecular orbital (HOMO) develops a p-orbital character, which is consistent with the interpretation of the π-bond moving to become a lone pair on the back phosphorus. The lowest unoccupied molecular orbital (LUMO) of the transition state shows a clear overlap between the π^* orbitals of disappearing π-bonds. This overlap appears along the new formed σ-bond. The HOMO of the final product shows a clear p-orbital on the back phosphorus and some σ-bond character along the newly formed bonds.

The barriers for these mechanisms starting from even-numbered chains P_{10}–P_{16} are summarized in Scheme 2c. Although there is no consistent trend for which pathway is preferred, both mechanisms have activation energies below 20 kcal/mol and so would be plausible even at low temperatures. Continued addition of P_2 units could result in increasingly long "ladder-like" structures. Other reaction paths following P_2 addition were considered; in particular the bicyclic intermediate (the third structure in Scheme 2a) bears resemblance to P_6a and Ahlrichs' P_{10}, both of which were the most stable isomers for their size. An alternate product (Scheme 2d, product A) would contain only σ-bonds and is more stable by 1.1 kcal/mol compared to the "ladder" motif. However, an attempt to locate the TS for Scheme 2d, product A instead led to product B consisting of white P and P_8b with a much higher activation energy than the final reaction in Scheme 2a. The reverse of this reaction, with a barrier of 17.5 kcal/mol (ΔE_{rxn}= −3.7 kcal/mol), could also reasonably be part of the oligomerization process if white P were present.

From the structures in Scheme 2c, pathways to red P chains were modeled by adding a bridging P_2 on top of the ladder. Scheme 3a shows an addition of diphosphorus on top of two σ-bonds, while Scheme 3b shows the formation of a cuneane-like structure can that could occur after an addition of diphosphorus at a terminating π-bonds. These steps have similar barriers to the reactions in Scheme 2 However, these mechanisms involve multiple endothermic steps and rate limiting barriers of >34 kcal/mol in the elementary step where the bridging P_2 completes the cage unit, cleaving a ladder σ-bond in the process. While some experimental conditions involving red P production are known to happen at high temperatures, this barrier is larger than most steps studied so far. These findings initially suggested that diphosphorus addition at σ-bonds would be mechanistically avoided.

Low-Energy Pathway for P–P σ-Bond Activation. Cuneane P_8 is clearly a very stable minimum on the potential energy surface of P clusters, and it showed little reactivity in the nanoreactor simulations. As in Scheme 1, the activation energy of adding P_2 to cuneane P_8 was found to be 42.9 kcal/mol in the nanoreactor. Inspired by the pseudopericyclic reactions at π-bonds, a new mechanistic path to larger P clusters was found. Addition of P_2 at the three-membered rings on cuneane P_8 have surprisingly low reaction barriers (16.0 kcal/mol) despite the occurrence of σ-bond cleavage (Scheme 3c). The resulting cluster is P_{10}b, or Jones' P_{10}, which is significant as Jones' P_{10} can be considered as one unit of red P. Diphosphorus additions at other atoms on cuneane P_8 were also considered (Scheme 3d–f). These have higher barriers (Scheme 3d,e), are significantly

Scheme 3. Cleavage of σ-Bonds with P–P π-Bonds[a]

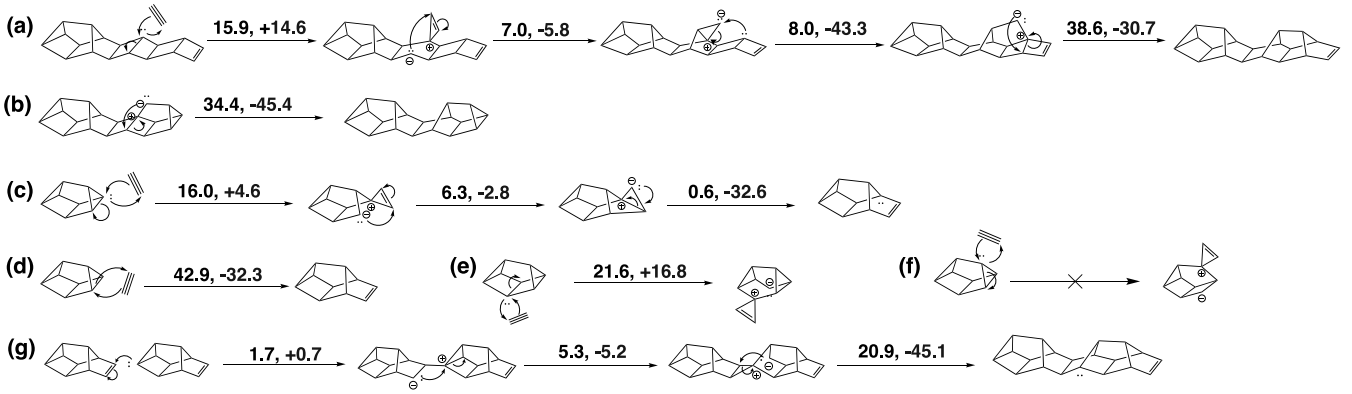

[a](a, b) Energetically costly addition of diphosphorus at ladder σ-bonds. (c) Pseudopericyclic addition of diphosphorus at three-membered ring σ-bonds of cuneane P_8. (d–f) Other possible P_2 additions to σ-bonds of cuneane P_8. (g) Oligomerization of Jones' P_{10} through σ-bond cleavage.

https://doi.org/10.1021/acs.inorgchem.4c02299
Inorg. Chem. 2024, 63, 19074–19086

more endothermic (Scheme 3e), or were unable to be characterized with our methods (Scheme 3f). Addition at the three-membered rings of cuneane P_8 (Scheme 3c) may be more favorable due to the formation of a five-membered ring in the intermediate simultaneous with the breaking of a four-member ring. Overall, this indicates that Jones' P_{10} would be the favored product between cuneane P_8 and P_2 (Figure 6).

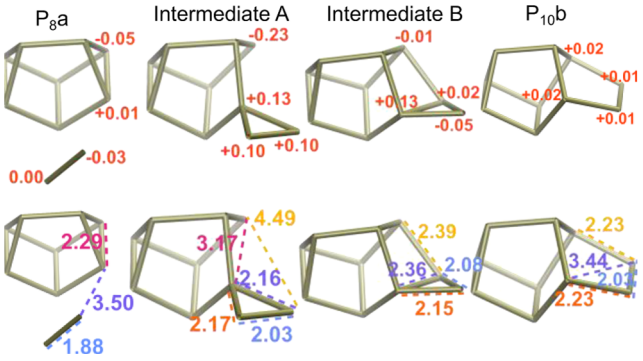

Figure 6. RESP charges (top) and bond distances (Å, bottom) for the reaction in Scheme 3c. All atoms without charges listed are smaller in magnitude than 0.05 a. u.

Similar to P_2 addition of P_{10}, the LUMO (Figure 7) for the sequence in Scheme 3c shows π^* character. In TS1, the π

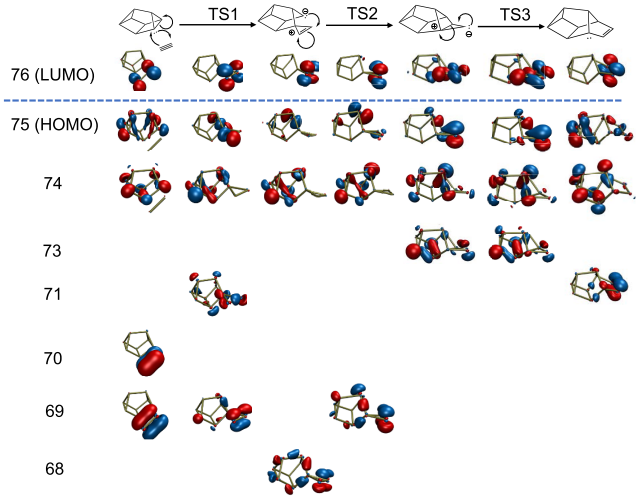

Figure 7. Relevant molecular orbitals for the addition of diphosphorus to cuneane P_8.

character of MO 70 starts to disappear as it approaches p-orbital lone-pair like character of P_{10} (MO 71). As with the P_2 addition to a π-bond in Figure 5, the HOMO and second HOMO display lone-pair character on the back phosphorus. This lone pair character diminishes in the last two reaction steps as that electron density forms new bonds. The second π-bond (MO 69) is conserved through the first reaction step, and becomes more localized on the rightmost phosphorus with lone-pair character through TS2 (MO 73). However, the π character is re-established through TS3 into the final product (MO 71).

This mechanism of using a π-bond to cleave cuneane P_8 can be extrapolated to devise a mechanism for oligomerization of P_{10} units (Scheme 3g). Here, the π-bond on one of the P_{10} units acts similarly to a P_2 and is attacked by the lone pair on the vertex of 3, 4, and 5-membered rings. Again, there is disappearance of the π character on the P_{10} unit (Figure 8, MO 126) as orbital density is developed like a lone pair (HOMO and second HOMO) first onto the P_{10} unit through TS1, and then onto the bottom-left phosphorus of P_8 through TS2. The lone pair character of the HOMO diminishes through TS3 as one σ-bond between the two units is broken and another is formed (MO's 113−115, 127).

These mechanisms generally proceed through three-membered cyclic, zwitterionic intermediate before rearranging to the tubular structure of red P. However, Kollman RESP charge calculations show more nuance in these intermediates (Figure 6). It seems that 3-member rings delocalize electron density. The quaternary phosphorus in Intermediate A is expected to show a distinct positive charge. However, the whole 3-member ring shows a significant positive charge (>0.10 a.u.). The lengths of the bonds in this ring also indicate delocalization as the newly formed single bonds (orange and purple) are not as long as typical P−P single bonds (>2.2 Å). In Intermediate B, the expected single bonds of the secondary phosphorus (blue and orange) are 2.08 and 2.15 Å, closer to the length of a typical P═P double bond (2.03 Å). The lack of a distinct negative charge on the secondary phosphorus also hints at the delocalized nature. Bond lengths and RESP charges for the dimerization reaction can be found in Figures S4 and S5, and similar patterns can be observed. The seeming tendency for electron delocalization in three-member rings is likely a contributing factor in the high occurrence and unusual stability they show in phosphorus clusters.

Nonetheless, the formal charges used to represent the work herein are still a useful heuristic for communicating mechanism and electron movement as shown in the MO's. With the reactions in Schemes 1 and 3c leading to the formation of P_{10}b and this oligomerization step of P_{10}b, a pathway to red P chains is clear starting from P_2. This pathway is summarized in Scheme 4. On path from the P_6b (C_{2v}) Dewar benzene structure (blue), another path from the P_ba benzavalene isomer (pink path), and another path from P_6f (gold path). The pink versus orange pathway depends on the orientation of the diphosphorus unit as it approaches P_4b. The pink path has the largest single reaction step barrier of 35.5 kcal/mol−plausible at some experimental temperatures (>275 °C), and seemingly necessary as no paths with smaller barriers were found that lead out from this P_6 global minimum. The orange path is an alternative path from P_4b that has no barriers larger than 25 kcal/mol. The blue pathway has similar barriers, but requires adding a P_2 unit to a less stable isomer of P_6.

Harmonic Free Energy Corrections May Not Be Sufficiently Accurate. To fully assess the plausibility of these pathways, evaluating the activation free energies is required. We computed the free energy barriers and reaction free energies using the harmonic approximation at 500 K. While the relative size of most reactions steps and barriers remained largely the same, bimolecular steps involving P_2 additions had consistently higher activation free energies by about 10−20 kcal/mol compared to the electronic activation energies (SI, Figure S2). This resulted in some key steps of the mechanism with barriers upward of 40+ kcal/mol and positive reaction free energies of almost 30 kcal/mol, which would not support the proposed mechanism.

However, the methods used to calculate free energies may not be appropriate for this system, as ideal gas approximations begin to break down with heavier and larger species. Additionally,

https://doi.org/10.1021/acs.inorgchem.4c02299
Inorg. Chem. 2024, 63, 19074−19086

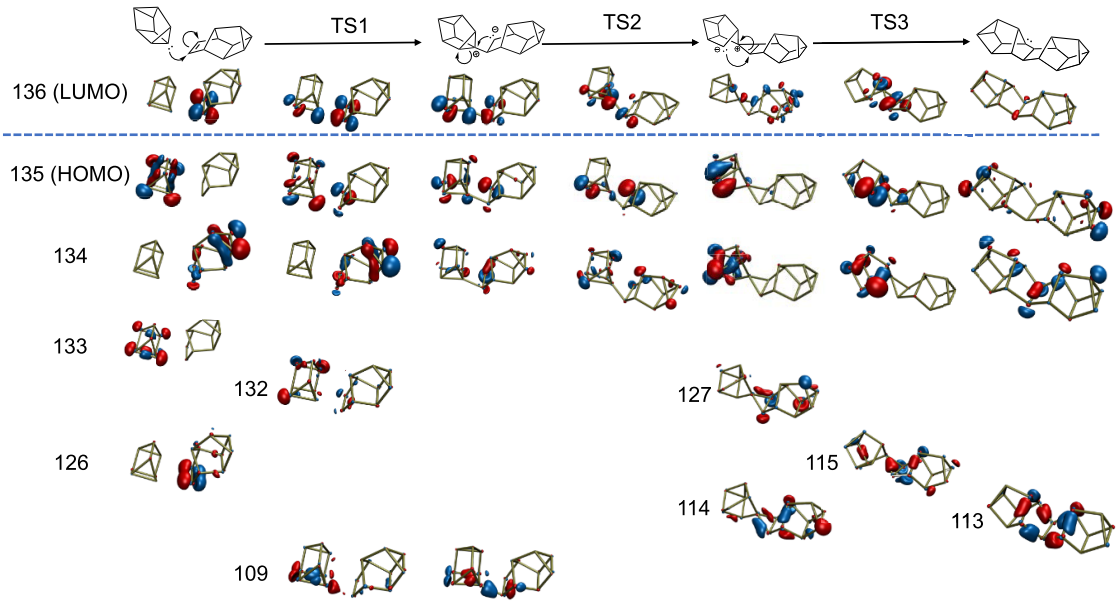

Figure 8. Relevant molecular orbitals for the dimerization of two cuneane P_8 units of red P.

Scheme 4. Electronic Potential Energy Surface of the Calculated Pathways from Diphosphorus[a] to a Unit of Red Phosphorus

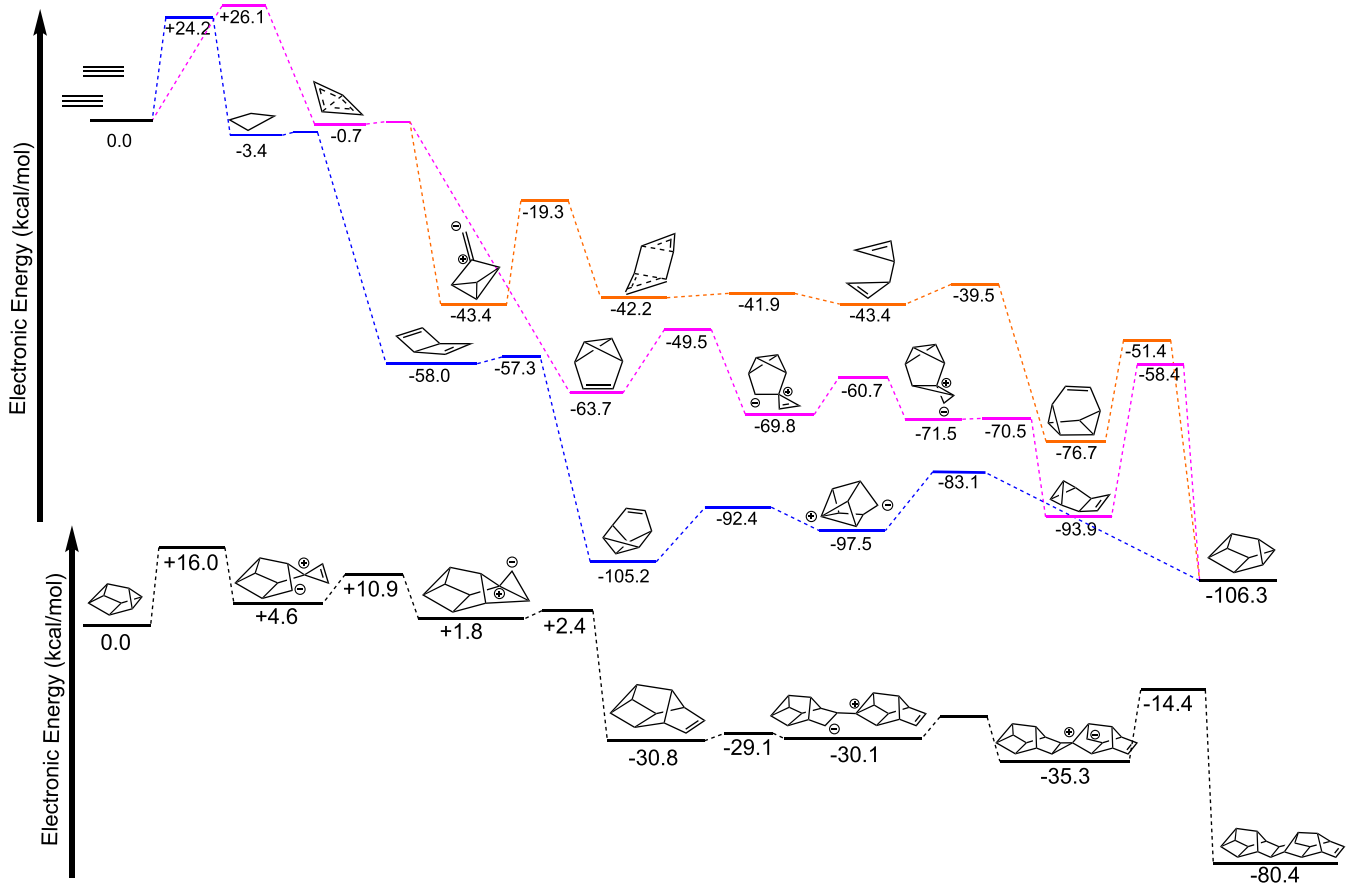

[a]Disphosphorus from addition steps are implied but not explicitly shown.

further investigations of the normal modes along the free energy surface revealed that the transition state structures for many of the diphosphorus addition steps contain a large number of low frequency vibrations corresponding to large amplitude motion. These motions are not properly described by a harmonic potential as typically done. To more rigorously characterize the free energy surface of diphosphorus additions, ab initio metadynamics were used as the method of choice.

Due to the high computational cost and the challenges involved in defining an appropriate collective variable (CV) for

https://doi.org/10.1021/acs.inorgchem.4c02299
Inorg. Chem. 2024, 63, 19074−19086

many of the reactions, we chose to study a single reaction, that of P_2 addition to Jones' P_{10}. In this reaction, the CV was chosen as the distance between a chosen P atom on the diphosphorus (P_A) and the atom labeled P_1 on the π-bond of P_{10} (Jones' isomer). The free energy simulation results using three different initial conditions are shown in Figure 9 and Table 1. The results

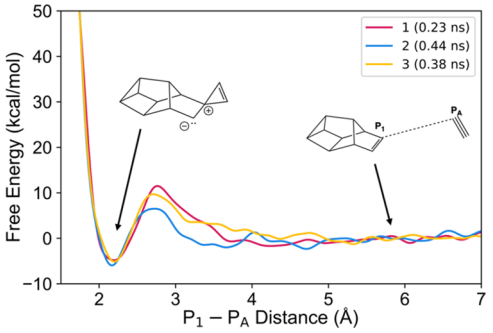

Figure 9. Free energy surface from metadynamics simulations for the P_2 addition to Jones' P_{10}.

Table 1. Free Energies and Barriers Generated from Metadynamics Simulations of $P10_b$ and P_2

	free energy barrier (kcal/mol)	reaction free energy (kcal/mol)
1 (0.23 ns)	11.5	−4.83
2 (0.44 ns)	6.51	−5.96
3 (0.38 ns)	9.71	−5.13

suggest that the free energy barrier is in the range of 6−12 kcal/mol, much lower than the harmonic approximation result (26.6 kcal/mol). The reaction free energies have good agreement, ranging from −5.96 to −4.83 kcal/mol, significantly lower than the harmonic approximation of +9.92 kcal/mol. To summarize, these free energy simulations strongly suggest that the harmonic approximations are overestimating the barrier height and reaction free energies for P_2 addition reactions.

CONCLUSIONS

From the data gathered, a plausible mechanism for how diphosphorus oligomerizes to red P clusters can be proposed. Our mechanism suggests that diphosphorus units tend to add to clusters at π-bonds and weak σ-bonds through three membered ring intermediates. Downhill paths through P_6 and P_8 clusters eventually result in P_{10} clusters that may oligomerize into various red P forms, with forms IV and V consisting of repetitions of said P_{10} clusters. This mechanism has the largest barrier of 24.2 kcal/mol at the start with two diphosphorus units coming together to form a P_4 species. Our methods of choice are supported by free energy simulations and multireference methods. While this study has largely focused on closed-shell species, more work can be done to explore open-shell mechanisms or mechanisms that involve ionic species.

Looking forward, another key mechanistic step that was not explored was the formation of P_{11} red P subunits by cross-linking P_{10} subunits with P_2. We anticipate that similar diphosphorus addition steps as the ones found here could play a part in the reaction pathway. Additionally, investigating paths with open-shell methods or ionic species could open a new realm of possibilities toward the formation of red P. Electron paramagnetic resonance analysis of the formation of red P could provide insights if radical formation is a crucial step in this process. Additionally, nuclear magnetic resonance could be of

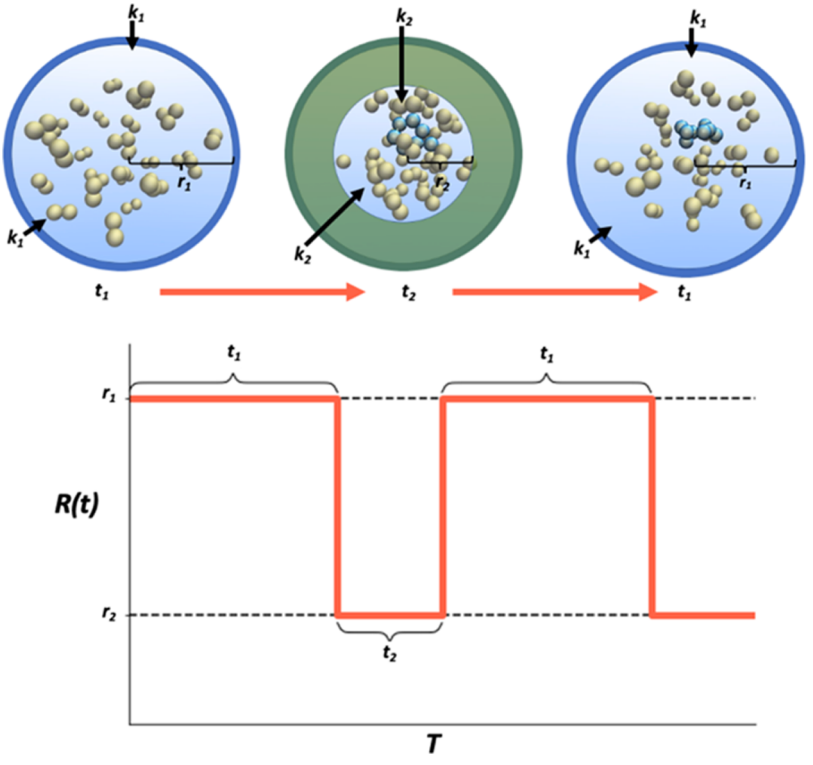

Figure 10. Nanoreactor oscillates between two boundary potentials. During t_2-intervals with the more restricted boundary potential, molecules outside the r_2-sphere are accelerated inward, inducing collisions and reactions. This process repeats as the molecules relax into the r_1-sphere during the t_1-intervals.

https://doi.org/10.1021/acs.inorgchem.4c02299
Inorg. Chem. 2024, 63, 19074−19086

some use in determining the ring size of intermediate species during oligomerization. Finally, our findings have also demonstrated the ability of the ab initio nanoreactor to inspire unique chemical hypotheses from the ground up. This suggests that further applications of the nanoreactor may be successful in generating reaction networks in systems that do not follow conventional rules, such as reactions dominated by noncarbon elements, ions, and/or radicals.

COMPUTATIONAL METHODS

The bulk of the calculations in this paper are in two categories—(1) the ab initio nanoreactor simulations for reaction discovery, and (2) conventional hypothesis testing involving the modeling and optimization of energy minima, transition states (TSs), and minimum energy paths (MEPs). The nanoreactor simulations were started from geometries consisting of P_2 molecules and P_2/P_4 mixtures for consistency with experimental demonstration of red P oligomerization from diphosphorus.[16−18] The reactions that are observed in the nanoreactor trajectories were converted into optimized MEPs in an automated procedure called energy refinement.[112] Furthermore, the study of the nanoreactor pathways helped to inspire chemically similar mechanistic hypotheses that were not directly observed in the trajectories; these we modeled and investigated "manually". We also incorporated potentially important reaction intermediates into the starting species of further nanoreactor simulations. In this way, the development of the reaction network involved several rounds of feedback between reaction discovery and hypothesis testing.

The ab initio nanoreactor simulations generally consisted of a number of randomly positioned and oriented P_2 units and other small P clusters with a total of 40−80 atoms. Due to the exploratory nature of these simulations, various combinations of simulation parameters were employed as described in the Supporting Information (Table S3). A representative simulation used the B3LYP hybrid density functional with the 6-31G* basis set and DFT-D3 dispersion correction, with the simulation time step set to 1 fs and a Langevin thermostat set to 1000 K and a damping time of 0.150 ps. Each simulation was propagated for an average of 20 ps. The simulations were carried out with the TeraChem[115−119] quantum chemistry software and initial conditions were generated using the PackMol[120] software.

The accelerated reactivity is generated through the combination of high temperature—which is close to the experimental conditions of red P formation—and a time-dependent external potential that is the nanoreactor's distinguishing feature (eq 1).

$$V(r,t) = \frac{m}{2}k(t)\rho(t)^2; \quad \rho = \begin{cases} r - R(t) & \text{if } r > R(t) \\ 0 & \text{otherwise} \end{cases}$$

$$k(t), R(t) = \begin{cases} k_1, R_1 & \text{if } t \bmod (t_1 + t_2) < t_1 \\ k_2, R_2 & \text{otherwise} \end{cases} \quad (1)$$

Here, m is the atomic mass, R_1 and R_2 are radius parameters ($R_2 < R_1$), and k_1 and k_2 are force constants. Equation 1 describes a flat-bottomed harmonic boundary potential with time-dependent parameters in which molecules are free to move within a sphere of R_1 for some time period t_1. After period t_1, the radius of the spherical region with zero potential shrinks to R_2; atoms outside of this radius are uniformly accelerated inward due to the mass-weighted force. The oscillating action induces high-velocity collisions that increase the number of observed reactions (Figure 10). Different combinations of the boundary potential parameters were tried to optimize the frequency of observing reactions that gave chemically reasonable activation barriers after energy refinement; recommended values are given in Rows 4 and 5 of Table S3.

Reactions observed in the nanoreactor trajectories were automatically identified and extracted from the trajectory, then input into an energy refinement procedure[112] in which the reactant, product, and transition state structures were optimized. This was followed by vibrational analysis of the TS structure and intrinsic reaction coordinate (IRC) calculations to verify the correctness of the MEP.[121] These calculations were performed at a higher level of theory compared to the nanoreactor simulations, namely the ωB97X-D3 range-separated functional[122] and the def-TZVP basis set.[123] This density functional has been benchmarked against gold standards (CCSDT(T)) and showed a mean absolute errors of 2.1 and 3.0 kcal/mol for reaction barriers and reaction energies, respectively.[124] It is also a computationally efficient choice, which is necessary due to the number of reactions explored and also the size of some of these systems (300+ electrons). Therefore, it is a reasonable choice for exploring our system. Approximate Gibbs free energies using the ideal gas/rigid rotor/harmonic oscillator approximation (abbreviated as "harmonic approximation") were calculated with vibrational analysis of the transition state, product, and reactant structures. The optimizations were done in translation-rotation internal coordinates with the geomeTRIC software interfaced with TeraChem.[125]

We also performed metadynamics simulations of selected reactions to assess the margin of error of the harmonic approximation for Gibbs free energies, particularly for bimolecular association reactions. Well-tempered metadynamics simulations were carried out using TeraChem with the PlumEd[126−128] plug-in, the ωB97X-D3 functional,[122] and the def-TZVP Gaussian basis set.[123] Simulations used a time step of 1 fs and were propagated for 500 ps. The Langevin thermostat was set to 500 K with a damping time of 150 fs. A bias factor of 5 was used with initial Gaussian height of 0.001 au, approximately 2% of the energy barrier, with a new biasing potential added every 100 fs. The collective variable was chosen to be the distance between the two phosphorus atoms forming a bond in the reaction of interest; a repulsive potential was placed at 15.0 Bohr.

ASSOCIATED CONTENT

Supporting Information

The Supporting Information is available free of charge at https://pubs.acs.org/doi/10.1021/acs.inorgchem.4c02299.

Free energy comparisons; nanoreactor parameters; multireference schemes; *xyz* coordinates (PDF)

AUTHOR INFORMATION

Corresponding Authors

Nathan D. Yoshino − *Department of Chemistry, University of California, Davis, Davis, California 95616, United States*; Email: ndyoshino@ucdavis.edu

Lee-Ping Wang − *Department of Chemistry, University of California, Davis, Davis, California 95616, United States*; orcid.org/0000-0003-3072-9946; Email: leeping@ucdavis.edu

Complete contact information is available at: https://pubs.acs.org/10.1021/acs.inorgchem.4c02299

Author Contributions

The manuscript was written through contributions of all authors. All authors have given approval to the final version of the manuscript.

Notes

The authors declare no competing financial interest.

ACKNOWLEDGMENTS

We thank Kit Cummins for inspiring this project and initial guidance in addition to his former students Tiansi Xin and Mike Geeson for their feedback on this work and manuscript.

REFERENCES

(1) Kolodiazhnyi, O. I. Phosphorus Compounds of Natural Origin: Prebiotic, Stereochemistry, Application. *Symmetry* **2021**, *13* (5), No. 889.

(2) Schrodter, K.; Bettermann, G.; Staffel, T.; Wahl, F.; Klein, T.; Hofmann, T. Industrial Phosphorus. In *Ullman's Encyclopedia of Industrial Chemistry*; Wiley, 2012; pp 503−519.
(3) Aparna, A. R.; Brahmajirao, V.; Karthikeyan, T. V. Review on Synthesis and Characterization of Gallium Phosphide. *Procedia Mater. Sci.* **2014**, *6*, 1650−1657.
(4) Sahrawat, K. L.; Abekoe, M. K.; Diatta, S. Application of Inorganic Phosphorus Fertilizer. In *Sustaining Soil Fertility in West Africa*, SSSA Special Publications; Wiley, 2015; p 225.
(5) Rumble, J. R. *CRC Handbook of Chemistry and Physics*, 102nd ed.; CRC Press/Taylor & Francis: Boca Raton, FL, 2021.
(6) Hultgren, R.; Gingrich, N. S.; Warren, B. E. The Atomic Distribution in Red and Black Phosphorus and the Crystal Structure of Black Phosphorus. *J. Chem. Phys.* **1935**, *3* (6), 351−355.
(7) Smith, A. J.; Roth, W. L.; DeWitt, T. W. Polymorphism of Red Phosphorus. *J. Am. Chem. Soc.* **1947**, *69* (11), 2881−2885.
(8) Transue, W. J.; Velian, A.; Nava, M.; Martin-Drumel, M. A.; Womack, C. C.; Jiang, J.; Hou, G. L.; Wang, X. Bin.; McCarthy, M. C.; Field, R. W.; Cummins, C. C. A Molecular Precursor to Phosphaethyne and Its Application in Synthesis of the Aromatic 1,2,3,4-Phosphatriazolate Anion. *J. Am. Chem. Soc.* **2016**, *138* (21), 6731−6734.
(9) Geeson, M. B.; Cummins, C. C. Phosphoric Acid as a Precursor to Chemicals Traditionally Synthesized from White Phosphorus. *Science* **2018**, *359* (6382), 1383−1385.
(10) Pham Minh, D.; Ramaroson, J.; Nzihou, A.; Sharrock, P. One-Step Synthesis of Sodium Trimetaphosphate ($Na_3P_3O_9$) from Sodium Chloride and Orthophosphoric Acid. *Ind. Eng. Chem. Res.* **2012**, *51* (10), 3851−3854.
(11) Geeson, M. B.; Cummins, C. C. Let's Make White Phosphorus Obsolete. *ACS Cent. Sci.* **2020**, *6* (6), 848−860.
(12) Popp, F. D.; McEwen, W. E. Polyphosphoric Acids As A Reagent In Organic Chemistry. *Chem. Rev.* **1958**, *58* (2), 321−401.
(13) Scheschkewitz, D. A Convenient P-Source. *Nat. Chem.* **2020**, *12* (9), 785−787.
(14) Frenette, B. L.; Trach, J.; Ferguson, M. J.; Rivard, E. Frustrated Lewis Pair Adduct of Atomic P(−1) as a Source of Phosphinidenes (PR), Diphosphorus (P_2), and Indium Phosphide. *Angew. Chem., Int. Ed.* **2023**, *62* (10), No. e202218587, DOI: 10.1002/anie.202218587.
(15) Tofan, D.; Cummins, C. C. Photochemical Incorporation of Diphosphorus Units into Organic Molecules. *Angew. Chem., Int. Ed.* **2010**, *49* (41), 7516−7518.
(16) Rathenau, G. Optische Und Photochemische Versuche Mit Phosphor. *Physica* **1937**, *4* (6), 503−514.
(17) Melville, H. W. The Photochemistry of Phosphine. *Proc. R. Soc. London, Ser. A* **1932**, *138* (836), 374−395.
(18) Melville, H. W.; Gray, S. C. Polymerization of Phosphorus. *Trans. Faraday Soc.* **1936**, *32*, 271−285.
(19) Ruck, M.; Hoppe, D.; Wahl, B.; Simon, P.; Wang, Y.; Seifert, G. Fibrous Red Phosphorus. *Angew. Chem., Int. Ed.* **2005**, *44* (46), 7616−7619.
(20) Thurn, H.; Krebs, H. Über Struktur Und Eigenschaften Der Halbmetalle. XXII. Die Kristallstruktur Des Hittorfschen Phosphors. *Acta Crystallogr., Sect. B: Struct. Crystallogr. Cryst. Chem.* **1969**, *25* (1), 125−135.
(21) Fasol, G.; Cardona, M.; Hönle, W.; von Schnering, H. G. Lattice Dynamics of Hittorf's Phosphorus and Identification of Structural Groups and Defects in Amorphous Red Phosphorus. *Solid State Commun.* **1984**, *52* (3), 307−310.
(22) Scheer, M.; Balázs, G.; Seitz, A. P_4 Activation by Main Group Elements and Compounds. *Chem. Rev.* **2010**, *110* (7), 4236−4256.
(23) Fung, C. M.; Er, C. C.; Tan, L. L.; Mohamed, A. R.; Chai, S. P. Red Phosphorus: An Up-and-Coming Photocatalyst on the Horizon for Sustainable Energy Development and Environmental Remediation. *Chem. Rev.* **2022**, *122* (3), 3879−3965.
(24) Tian, H.; Wang, J.; Lai, G.; Dou, Y.; Gao, J.; Duan, Z.; Feng, X.; Wu, Q.; He, X.; Yao, L.; Zeng, L.; Liu, Y.; Yang, X.; Zhao, J.; Zhuang, S.; Shi, J.; Qu, G.; Yu, X. F.; Chu, P. K.; Jiang, G. Renaissance of Elemental Phosphorus Materials: Properties, Synthesis, and Applications in Sustainable Energy and Environment. *Chem. Soc. Rev.* **2023**, *52* (16), 5388−5484.
(25) Wang, F.; Ng, W. K. H.; Yu, J. C.; Zhu, H.; Li, C.; Zhang, L.; Liu, Z.; Li, Q. Red Phosphorus: An Elemental Photocatalyst for Hydrogen Formation from Water. *Appl. Catal., B* **2012**, *111*−*112*, 409−414.
(26) Wang, F.; Li, C.; Li, Y.; Yu, J. C. Hierarchical P/YPO4Microsphere for Photocatalytic Hydrogen Production from Water under Visible Light Irradiation. *Appl. Catal., B* **2012**, *119*−*120*, 267−272.
(27) Dang, H.; Dong, X.; Dong, Y.; Fan, H.; Qiu, Y. Enhancing the Photocatalytic H_2 Evolution Activity of Red Phosphorous by Using Noble-Metal-Free $Ni(OH)_2$ under Photoexcitation up to 700 Nm. *RSC Adv.* **2014**, *4* (84), 44823−44826.
(28) Cheng, Z.; Fang, W.; Zhao, T.; Fang, S.; Bi, J.; Liang, S.; Li, L.; Yu, Y.; Wu, L. Efficient Visible-Light-Driven Photocatalytic Hydrogen Evolution on Phosphorus-Doped Covalent Triazine-Based Frameworks. *ACS Appl. Mater. Interfaces* **2018**, *10* (48), 41415−41421.
(29) Chen, J.; Huang, S.; Long, Y.; Wu, J.; Li, H.; Li, Z.; Zeng, Y.-J.; Ruan, S. Fabrication of ZnO/Red Phosphorus Heterostructure for Effective Photocatalytic H_2 Evolution from Water Splitting. *Nanomaterials* **2018**, *8* (10), No. 835.
(30) Liu, E.; Qi, L.; Chen, J.; Fan, J.; Hu, X. In Situ Fabrication of a 2D Ni_2 P/Red Phosphorus Heterojunction for Efficient Photocatalytic H_2 Evolution. *Mater. Res. Bull.* **2019**, *115*, 27−36.
(31) Liu, Y.; Hu, Z.; Yu, J. C. Liquid Bismuth Initiated Growth of Phosphorus Microbelts with Efficient Charge Polarization for Photocatalysis. *Appl. Catal., B* **2019**, *247*, 100−106.
(32) Zhang, M.; Liu, J.; Liu, L.; Sun, K.; Liang, X.; Wan, J.; Fu, F. A New High-Yield Fabrication Approach for Porous Red Phosphorus Nanosheets Using N-Methyl-2-Pyrrolidone with Multiple Photocatalytic Reduction Applications. *Ceram. Int.* **2020**, *46* (14), 23165−23172.
(33) Wang, M.; Qin, Z.; Diao, Z.; Li, R.; Zhong, J.; Ma, D.; Chen, Y. Red Phosphorus/Carbon Nitride van Der Waals Heterostructure for Photocatalytic Pure Water Splitting under Wide-Spectrum Light Irradiation. *ACS Sustainable Chem. Eng.* **2020**, *8* (35), 13459−13466.
(34) Zhu, Y.; Lv, C.; Yin, Z.; Ren, J.; Yang, X.; Dong, C.-L.; Liu, H.; Cai, R.; Huang, Y.-C.; Theis, W.; Shen, S.; Yang, D. A [001]-Oriented Hittorf's Phosphorus Nanorods/Polymeric Carbon Nitride Heterostructure for Boosting Wide-Spectrum-Responsive Photocatalytic Hydrogen Evolution from Pure Water. *Angew. Chem., Int. Ed.* **2020**, *59* (2), 868−873.
(35) Jia, J.; Bai, X.; Zhang, Q.; Hu, X.; Liu, E.; Fan, J. Porous Honeycomb-like $NiSe_2$/Red Phosphorus Heteroarchitectures for Photocatalytic Hydrogen Production. *Nanoscale* **2020**, *12* (9), 5636−5651.
(36) Xu, M.; Jiang, L.; Wang, J.; Feng, S.; Tremblay, P. L.; Zhang, T. Efficient Photocatalytic Hydrogen Evolution with High-Crystallinity and Noble Metal-Free Red Phosphorus-CdS Nanorods. *Int. J. Hydrogen Energy* **2020**, *45* (35), 17354−17366.
(37) Guo, C.; Du, H.; Ma, Y.; Qi, K.; Zhu, E.; Su, Z.; Huojiaaihemaiti, M.; Wang, X. Visible-Light Photocatalytic Activity Enhancement of Red Phosphorus Dispersed on the Exfoliated Kaolin for Pollutant Degradation and Hydrogen Evolution. *J. Colloid Interface Sci.* **2021**, *585*, 167−177.
(38) Hu, L.; Xu, J.; Zhao, S.; Li, X.; Li, L.; Ran, L. Red/Black Phosphorus Z-Scheme Heterogeneous Junction Modulated by Co-MOF for Enhanced Photocatalytic Hydrogen Evolution. *Catal. Lett.* **2021**, *151* (9), 2658−2672.
(39) Chen, N.; Cao, J.; Guo, M.; Liu, C.; Lin, H.; Chen, S. Novel NiO/RP Composite with Remarkably Enhanced Photocatalytic Activity for H_2 Evolution from Water. *Int. J. Hydrogen Energy* **2021**, *46* (37), 19363−19372.
(40) Ansari, S. A.; Cho, M. H. Highly Visible Light Responsive, Narrow Band Gap TiO_2 Nanoparticles Modified by Elemental Red Phosphorus for Photocatalysis and Photoelectrochemical Applications. *Sci. Rep.* **2016**, *6*, No. 25405.
(41) Zhou, H.; Xu, S.; Zhang, D.; Chen, S.; Deng, J. One Step in Situ Synthesis of Core-Shell Structured Cr_2O_3:P@fibrous-Phosphorus

https://doi.org/10.1021/acs.inorgchem.4c02299
Inorg. Chem. 2024, 63, 19074−19086

Hybrid Composites with Highly Efficient Full-Spectrum-Response Photocatalytic Activities. *Nanoscale* **2017**, *9* (9), 3196−3205.
(42) Wang, J.; Pi, M.; Zhang, D.; Chen, S. The Visible-Light Photocatalytic Activity for Enhancing RhB Degradation and Hydrogen Evolution from $SrTiO_3$ Nanoparticles Decorated Red Phosphorus Nanorods as Photocatalysts. *J. Phys. D: Appl. Phys.* **2020**, *53* (8), No. 085501, DOI: 10.1088/1361-6463/ab58df.
(43) Athira, T. K.; Roshith, M.; Babu, T. G. S.; Kumar, D. V. R. Fibrous Red Phosphorus as a Non-Metallic Photocatalyst for the Effective Reduction of Cr(VI) under Direct Sunlight. *Mater. Lett.* **2021**, *283*, No. 128750.
(44) Wang, W.; Li, G.; An, T.; Chan, D. K. L.; Yu, J. C.; Wong, P. K. Photocatalytic Hydrogen Evolution and Bacterial Inactivation Utilizing Sonochemical-Synthesized g-C_3N_4/Red Phosphorus Hybrid Nanosheets as a Wide-Spectral-Responsive Photocatalyst: The Role of Type I Band Alignment. *Appl. Catal., B* **2018**, *238*, 126−135.
(45) Roshith, M.; Kumar, M. S.; Kumar, A. K. N.; Ramasubramanian, S.; Stanley, J.; Babu, T. G. S.; Kumar, D. V. R. Urchin-like Fibrous Red Phosphorus as an Efficient Photocatalyst for Solar-Light-Driven Disinfection of *E. Coli*. *J. Photochem. Photobiol., A* **2019**, *384*, No. 112034.
(46) Kaur, H.; Konkena, B.; Gabbett, C.; Smith, R.; McCrystall, M.; Tian, R.; Roy, A.; Carey, T.; Vega-Mayoral, V.; Nicolosi, V.; Coleman, J. N. Amorphous 2D-Nanoplatelets of Red Phosphorus Obtained by Liquid-Phase Exfoliation Yield High Areal Capacity Na-Ion Battery Anodes. *Adv. Energy Mater.* **2023**, *13* (6), No. 2203013, DOI: 10.1002/aenm.202203013.
(47) Kim, Y.; Park, Y.; Choi, A.; Choi, N. S.; Kim, J.; Lee, J.; Ryu, J. H.; Oh, S. M.; Lee, K. T. An Amorphous Red Phosphorus/Carbon Composite as a Promising Anode Material for Sodium Ion Batteries. *Adv. Mater.* **2013**, *25* (22), 3045−3049.
(48) Liu, W.; Ju, S.; Yu, X. Phosphorus-Amine-Based Synthesis of Nanoscale Red Phosphorus for Application to Sodium-Ion Batteries. *ACS Nano* **2020**, *14* (1), 974−984.
(49) Kong, W.; Xu, S.; Yin, J.; Yang, H.; Feng, W.; Cui, L.; Wen, Z. A Novel Red Phosphorus/Reduced Graphene Oxide-C_3N_4 Composite with Enhanced Sodium Storage Capability. *J. Electroanal. Chem.* **2021**, *902*, No. 115819.
(50) Zhu, Z.; Pei, Z.; Liu, B.; Sun, D.; Fang, Y.; Lei, X.; Liu, X.; Niu, S.; Pan, H.; Zhou, J.; Qian, Y.; Wang, G. Hierarchical Ion/Electron Networks Enable Efficient Red Phosphorus Anode with High Mass Loading for Sodium Ion Batteries. *Adv. Funct. Mater.* **2022**, *32* (16), No. 2110444.
(51) He, S.-A.; Liu, Q.; Cui, Z.; Xu, K.; Zou, R.; Luo, W.; Zhu, M. Red Phosphorus Anchored on Nitrogen-Doped Carbon Bubble-Carbon Nanotube Network for Highly Stable and Fast-Charging Lithium-Ion Batteries. *Small* **2022**, *18* (7), No. 2105866.
(52) Sun, Y.; Wu, Q.; Zhang, K.; Liu, Y.; Liang, X.; Xiang, H. A High Areal Capacity Sodium-Ion Battery Anode Enabled by a Free-Standing Red Phosphorus@N-Doped Graphene/CNTs Aerogel. *Chem. Commun.* **2022**, *58* (51), 7120−7123.
(53) Song, J.; Peng, X.; Liu, D.; Li, H.; Wu, M.; Fang, K.; Zhu, X.; Xiang, X.; Tang, H. On-Site Conversion Reaction Enables Ion-Conducting Surface on Red Phosphorus/Carbon Anode for Durable and Fast Sodium-Ion Batteries. *J. Energy Chem.* **2023**, *80*, 381−391.
(54) Luan, Q.; Xue, X.; Feng, H.; Tao, L.; Zhou, D.; Chen, T.; Tan, M.; Dong, W. In-Plane Carrier Regulation and Hydrogen Adsorption/Desorption Optimization of P_4 Molecule Anchored Vs-$ZnIn_2S_{4-x}$ for Improve Photocatalytic Activity. *Appl. Catal., B* **2023**, *337*, No. 122932.
(55) Huang, H.; Xie, D.; Zheng, Z.; Zeng, Y.; Xie, S.; Liu, P.; Zhang, M.; Wang, S.; Cheng, F. Recycled Graphite from Spent Lithium-Ion Batteries as a Conductive Framework Directly Applied in Red Phosphorus-Based Anodes. *ACS Appl. Mater. Interfaces* **2023**, *15* (45), 52686−52695.
(56) Baudler, M.; Glinka, K. Monocyclic and Polycyclic Phosphanes. *Chem. Rev.* **1993**, *93*, 1623−1667.
(57) Hennersdorf, F.; Weigand, J. J. A Tetracyclic Octaphosphane by Successive Addition, Inversion, and Condensation Reactions. *Angew. Chem., Int. Ed.* **2017**, *56* (27), 7858−7862.
(58) Hennersdorf, F.; Frötschel, J.; Weigand, J. J. Selective Derivatization of a Hexaphosphane from Functionalization of White Phosphorus. *J. Am. Chem. Soc.* **2017**, *139* (41), 14592−14604.
(59) Eilrich, V. J.; Grell, T.; Lönnecke, P.; Hey-Hawkins, E. Coordination Chemistry of Hepta-Tert-Butylnonaphosphane. *Dalton Trans.* **2022**, *51* (29), 10887−10897.
(60) Ziegler, C. G. P.; Maier, T. M.; Pelties, S.; Taube, C.; Hennersdorf, F.; Ehlers, A. W.; Weigand, J. J.; Wolf, R. Construction of Alkyl-Substituted Pentaphosphido Ligands in the Coordination Sphere of Cobalt. *Chem. Sci.* **2019**, *10* (5), 1302−1308.
(61) Gendy, C.; Valjus, J.; Roesler, R.; Tuononen, H. M. Haptotropism in a Nickel Complex with a Neutral, π-Bridging Cyclo-P_4 Ligand Analogous to Cyclobutadiene. *Angew. Chem., Int. Ed.* **2022**, *61* (18), No. e202115692, DOI: 10.1002/anie.202115692.
(62) Wang, S.; Sears, J. D.; Moore, C. E.; Rheingold, A. L.; Neidig, M. L.; Figueroa, J. S. Side-on Coordination of Diphosphorus to a Mononuclear Iron Center. *Science* **2022**, *375* (6587), 1393−1397.
(63) Edgar, M.; Elsegood, M. R. J.; Liu, P.; Miles, C. R.; Smith, M. B.; Wu, S. Dinuclear Palladium(II) and Platinum(II) Complexes of a Readily Accessible Bicyclic Diphosphane. *Eur. J. Inorg. Chem.* **2022**, *2022* (12), No. e202200017.
(64) Yang, C.; Jiang, X.; Chen, Q.; Leng, X.; Xiao, J.; Ye, S.; Deng, L. Signet-Ring-Shaped Octaphosphorus-Cobalt Complexes: Synthesis, Structure, and Functionalization Reactions with Carbene Analogs. *J. Am. Chem. Soc.* **2022**, *144* (45), 20785−20796.
(65) Senthil, S.; Gau, M. R.; Mindiola, D. J. A Contiguous Tricyclic $[P_6]_2$-Framework Spanning Across Two Vanadium(III) Centers. *Organometallics* **2023**, *42* (11), 1048−1051.
(66) Eilrich, V. J.; Hey-Hawkins, E. Cyclooligophosphanes and Their Coordination Chemistry. *Coord. Chem. Rev.* **2021**, *437*, No. 213749.
(67) Pauling, L.; Simonetta, M. Bond Orbitals and Bond Energy in Elementary Phosphorus. *J. Chem. Phys.* **1952**, *20* (1), 29−34.
(68) Baudler, M.; Ternberger, H.; Faber, W.; Hahn, J. Li_3P_7, Ein Polyphosphid Mit Fluktuierenden Bindungen: Synthese Aus P_2H_4 Und Überführung in P_7H_3. *Z. Naturforsch.* **1979**, *34*, 1690−1697.
(69) Baudler, M.; Faber, W. Einfache Darstellung von Trilithium-heptaphosphid Aus Farblosem Phosphor Und Lithiumdihydrogen-phosphid. *Chem. Ber.* **1980**, *113* (10), 3394−3395.
(70) Baudler, M.; Heumüller, R.; Langerbeins, K. Dilithium-Hydrogenheptaphosphid, $LiHP_7$ - Ein Teilmetalliertes Derivat von P_7H_3: Darstellung Und Strukturelle Charakterisierung. *Z. Anorg. Allg. Chem.* **1984**, *514*, 7−17.
(71) Baudler, M.; Heumüller, R.; Germeshausen, J.; Hahn, J. Dilithium-Dihydrogentetradecaphosphid, $Li_2H_2P_{14}$: Darstellung Und Strukturelle Charakterisierung. *Z. Anorg. Allg. Chem.* **1985**, *526*, 7−14.
(72) Baudler, M.; Heumüller, R. Lithium-Tetrahydrogenheptaphosphid Und Lithium-Octahydrogenheptaphosphid. *Z. Anorg. Allg. Chem.* **1988**, *559*, 49−56.
(73) Böcker, S.; Häser, M. Covalent Structures of Phosphorus: A Comprehensive Theoretical Study. *Z. Anorg. Allg. Chem.* **1995**, *621* (2), 258−286.
(74) Kerwin, L. Some Mass Spectrometric Data on Phosphorus. *Can. J. Phys.* **1954**, *32* (12), 757−758.
(75) Carette, J.-D.; Kerwin, L. Une Étude Du Phosphore Rouge Par Spectrométrie de Masse. *Can. J. Phys.* **1961**, *39*, 1300−1319.
(76) Kane, J. S.; Reynolds, J. H. Mass Spectrometer Study of the Vapors from Red Phosphorus and Arsenic. *J. Chem. Phys.* **1956**, *25* (2), 342−349.
(77) Smets, J.; Coppens, P.; Drowart, J. Photoionization with Mass Spectkometric Analysis of the Tetraphosphorus Molecule. *Chem. Phys.* **1977**, *20*, 243−251.
(78) Martin, T. P. Compound Clusters. *Z. Phys. D At., Mol. Clust.* **1986**, *3* (2), 211−217.
(79) Huang, R.; Li, H.; Lin, Z.; Yang, S. Experimental and Theoretical Studies of Small Homoatomic Phosphorus Clusters. *J. Phys. Chem. A* **1995**, *99* (5), 1418−1423.
(80) Chen, M. D.; Li, J. T.; Huang, R. B.; Zheng, L. S.; Au, C. T. Structure Prediction of Large Cationic Phosphorus Clusters. *Chem. Phys. Lett.* **1999**, *305* (5−6), 439−445.

(81) Sládková, K.; Houška, J.; Havel, J. Laser Desorption Ionization of Red Phosphorus Clusters and Their Use for Mass Calibration in Time-of-Flight Mass Spectrometry. *Rapid Commun. Mass Spectrom.* **2009**, *23* (19), 3114−3118.
(82) Kolářová, L.; Prokeš, L.; Kučera, L.; Hampl, A.; Peña-Méndez, E.; Vaňhara, P.; Havel, J. Clusters of Monoisotopic Elements for Calibration in (TOF) Mass Spectrometry. *J. Am. Soc. Mass Spectrom.* **2017**, *28* (3), 419−427.
(83) Trinquier, G.; Malrieu, J.; Daudley, J.-P. Ab Initio Study of the Regular Polyhedral Molecules N_4, P_4, As_4, N_8, P_8 and As_8. *Chem. Phys. Lett.* **1981**, *80* (3), 552−557.
(84) Ahlrichs, R.; Brode, S.; Ehrhardt, C. Theoretical Study of the Stability of Molecular P_2, P_4 (T_d), and P_8 (O_h). *J. Am. Chem. Soc.* **1985**, *107* (25), 7260−7264.
(85) Schiffer, H.; Ahlrichs, R.; Häser, M. Theoretical Investigation of next Neighbour Interactions and Ring Strain in Linear and Monocyclic Phosphanes. *Theor. Chim. Acta* **1989**, *75* (1), 1−10.
(86) Haeser, M.; Schneider, U.; Ahlrichs, R. Clusters of Phosphorus: A Theoretical Investigation. *J. Am. Chem. Soc.* **1992**, *114* (24), 9551−9559.
(87) Jones, R. O.; Hohl, D. Structure of Phosphorus Clusters Using Simulated Annealing - P_2 to P_8. *J. Chem. Phys.* **1990**, *92* (11), 6710−6721.
(88) Jones, R. O.; Seifert, G. Structure of Phosphorus Clusters Using Simulated Annealing. II. P_9, P_{10}, P_{11}, Anions P_4^{2-}, P_{10}^{2-}, P_{11}^{3-}, and Cations P_{N+} to N = 11. *J. Chem. Phys.* **1992**, *96* (10), 7564−7572.
(89) Ballone, P.; Jones, R. O. Density Functional Study of Phosphorus and Arsenic Clusters Using Local and Non Local Energy Functionals. *J. Chem. Phys.* **1994**, *100*, 4941−4946.
(90) Elliott, S. R.; D, J. C.; M, E. The Structure of Amorphous Phophorus. *J. Phys. Colloq.* **1985**, *46* (C8), 349−353.
(91) Haeser, M. Structural Rules of Phosphorus. *J. Am. Chem. Soc.* **1994**, *116* (15), 6925−6926.
(92) Häser, M.; Treutler, O. Calculated Properties of P_2, P_4, and of Closed-Shell Clusters up to P_{18}. *J. Chem. Phys.* **1995**, *102*, 3703−3711.
(93) Warren, D. S.; Gimarc, B. M. Valence Isomers of Benzene and Their Relationship to Isomers of Isoelectronic P_6. *J. Am. Chem. Soc.* **1992**, *114* (13), 5378−5385.
(94) Gimarc, B. M.; Warren, D. S. Relative Energies and Strain Energies of Proposed Structures for Octaphosphorus. *Inorg. Chem.* **1993**, *32* (9), 1850−1856.
(95) Warren, D. S.; Gimarc, B. M. Maximum Hardness in P_6 Isomers. *Int. J. Quantum Chem.* **1994**, *49* (3), 207−213.
(96) Chen, M. D.; Huang, R. B.; Zheng, L. S.; Au, C. T. The Prediction of Isomers for the Phosphorus Clusters P_7^+. *Main Group Met. Chem.* **1999**, *22* (8), 479−483.
(97) Chen, M. D.; Luo, H. B.; Liu, M. H.; Zhang, Q. E.; Au, C. T. A Theoretical Study of the Isomers of Phosphorus Clusters P_{11}, P_{11}^+ and P_{11}^-. *Main Group Met. Chem.* **2000**, *23* (7), 361−367.
(98) Chen, M. D.; Chen, Q. B.; Liu, J.; Zheng, L. S.; Zhang, Q. E.; Au, C. T. Parity Alternation of Ground-State P_n^- and P_N^+ (n = 3−15) Phosphorus Clusters. *J. Phys. Chem. A* **2007**, *111* (2), 216−222.
(99) Guo, L.; Wu, H.; Jin, Z. First Principles Study of the Evolution of the Properties of Neutral and Charged Phosphorus Clusters. *J. Mol. Struct.: THEOCHEM* **2004**, *677*, 59−66.
(100) Xue, T.; Luo, J.; Shen, S.; Li, F.; Zhao, J. Lowest-Energy Structures of Cationic P_{2m+1}^+ (m = 1−12) Clusters from First-Principles Simulated Annealing. *Chem. Phys. Lett.* **2010**, *485* (1−3), 26−30.
(101) Zimmerman, P. M. Navigating Molecular Space for Reaction Mechanisms: An Efficient, Automated Procedure. *Mol. Simul.* **2015**, *41* (1−3), 43−54.
(102) Dewyer, A. L.; Zimmerman, P. M. Finding Reaction Mechanisms, Intuitive or Otherwise. *Org. Biomol. Chem.* **2017**, *15* (3), 501−504.
(103) Jafari, M.; Zimmerman, P. M. Uncovering Reaction Sequences on Surfaces through Graphical Methods. *Phys. Chem. Chem. Phys.* **2018**, *20* (11), 7721−7729.
(104) Matheu, D. M.; Dean, A. M.; Grenda, J. M.; Green, W. H. Mechanism Generation with Integrated Pressure Dependence: A New Model for Methane Pyrolysis. *J. Phys. Chem. A* **2003**, *107* (41), 8552−8565.
(105) Gao, C. W.; Allen, J. W.; Green, W. H.; West, R. H. Reaction Mechanism Generator: Automatic Construction of Chemical Kinetic Mechanisms. *Comput. Phys. Commun.* **2016**, *203*, 212−225.
(106) Bergeler, M.; Simm, G. N.; Proppe, J.; Reiher, M. Heuristics-Guided Exploration of Reaction Mechanisms. *J. Chem. Theory Comput.* **2015**, *11* (12), 5712−5722.
(107) Martínez-Núñez, E. An Automated Method to Find Transition States Using Chemical Dynamics Simulations. *J. Comput. Chem.* **2015**, *36* (4), 222−234.
(108) Martínez-Núñez, E. An Automated Transition State Search Using Classical Trajectories Initialized at Multiple Minima. *Phys. Chem. Chem. Phys.* **2015**, *17* (22), 14912−14921.
(109) Varela, J. A.; Vázquez, S. A.; Martínez-Núñez, E. An Automated Method to Find Reaction Mechanisms and Solve the Kinetics in Organometallic Catalysis. *Chem. Sci.* **2017**, *8* (5), 3843−3851.
(110) Pietrucci, F.; Andreoni, W. Graph Theory Meets *Ab Initio* Molecular Dynamics: Atomic Structures and Transformations at the Nanoscale. *Phys. Rev. Lett.* **2011**, *107* (8), No. 085504.
(111) Wang, L. P.; Titov, A.; McGibbon, R.; Liu, F.; Pande, V. S.; Martínez, T. J. Discovering Chemistry with an *Ab Initio* Nanoreactor. *Nat. Chem.* **2014**, *6* (12), 1044−1048.
(112) Wang, L. P.; McGibbon, R. T.; Pande, V. S.; Martinez, T. J. Automated Discovery and Refinement of Reactive Molecular Dynamics Pathways. *J. Chem. Theory Comput.* **2016**, *12* (2), 638−649.
(113) Wang, L. P.; Tofan, D.; Chen, J.; Van Voorhis, T.; Cummins, C. C. A Pathway to Diphosphorus from the Dissociation of Photoexcited Tetraphosphorus. *RSC Adv.* **2013**, *3* (45), 23166−23171.
(114) Vitillo, J. G.; Cramer, C. J.; Gagliardi, L. Multireference Methods Are Realistic and Useful Tools for Modeling Catalysis. *Isr. J. Chem.* **2022**, *62* (1−2), No. e202100136.
(115) Ufimtsev, I. S.; Martínez, T. J. Quantum Chemistry on Graphical Processing Units. 1. Strategies for Two-Electron Integral Evaluation. *J. Chem. Theory Comput.* **2008**, *4* (2), 222−231.
(116) Ufimtsev, I. S.; Martinez, T. J. Quantum Chemistry on Graphical Processing Units. 2. Direct Self-Consistent-Field Implementation. *J. Chem. Theory Comput.* **2009**, *5* (4), 1004−1015.
(117) Ufimtsev, I. S.; Martinez, T. J. Quantum Chemistry on Graphical Processing Units. 3. Analytical Energy Gradients, Geometry Optimization, and First Principles Molecular Dynamics. *J. Chem. Theory Comput.* **2009**, *5* (10), 2619−2628.
(118) Snyder, J. W.; Curchod, B. F. E.; Martínez, T. J. GPU-Accelerated State-Averaged Complete Active Space Self-Consistent Field Interfaced with *Ab Initio* Multiple Spawning Unravels the Photodynamics of Provitamin D3. *J. Phys. Chem. Lett.* **2016**, *7* (13), 2444−2449.
(119) Liu, F.; Sanchez, D. M.; Kulik, H. J.; Martínez, T. J. Exploiting Graphical Processing Units to Enable Quantum Chemistry Calculation of Large Solvated Molecules with Conductor-like Polarizable Continuum Models. *Int. J. Quantum Chem.* **2019**, *119* (1), No. e25760.
(120) Martínez, L.; Andrade, R.; Birgin, E. G.; Martínez, J. M. PACKMOL: A Package for Building Initial Configurations for Molecular Dynamics Simulations. *J. Comput. Chem.* **2009**, *30* (13), 2157−2164.
(121) Fukui, K. The Path of Chemical Reactions - the IRC Approach. *Acc. Chem. Res.* **1981**, *14* (12), 363−368.
(122) Lin, Y. S.; Li, G.-D.; Mao, S. P.; Chai, J.-D. Long-Range Corrected Hybrid Density Functionals with Improved Dispersion Corrections. *J. Chem. Theory Comput.* **2013**, *9* (1), 263−272.
(123) Eichkorn, K.; Weigend, F.; Treutler, O.; Ahlrichs, R. Auxiliary Basis Sets for Main Row Atoms and Transition Metals and Their Use to Approximate Coulomb Potentials. *Theor. Chem. Acc.* **1997**, *97* (1−4), 119−124.
(124) Goerigk, L.; Hansen, A.; Bauer, C.; Ehrlich, S.; Najibi, A.; Grimme, S. A Look at the Density Functional Theory Zoo with the Advanced GMTKN55 Database for General Main Group Thermo-

https://doi.org/10.1021/acs.inorgchem.4c02299
Inorg. Chem. 2024, 63, 19074−19086

chemistry, Kinetics and Noncovalent Interactions. *Phys. Chem. Chem. Phys.* **2017**, *19* (48), 32184−32215.
(125) Wang, L. P.; Song, C. Geometry Optimization Made Simple with Translation and Rotation Coordinates. *J. Chem. Phys.* **2016**, *144* (21), No. 214108, DOI: 10.1063/1.4952956.
(126) Bonomi, M.; Branduardi, D.; Bussi, G.; Camilloni, C.; Provasi, D.; Raiteri, P.; Donadio, D.; Marinelli, F.; Pietrucci, F.; Broglia, R. A.; Parrinello, M. PLUMED: A Portable Plugin for Free-Energy Calculations with Molecular Dynamics. *Comput. Phys. Commun.* **2009**, *180* (10), 1961−1972.
(127) Tribello, G. A.; Bonomi, M.; Branduardi, D.; Camilloni, C.; Bussi, G. PLUMED 2: New Feathers for an Old Bird. *Comput. Phys. Commun.* **2014**, *185* (2), 604−613.
(128) The PLUMED Consortium. Promoting Transparency and Reproducibility in Enhanced Molecular Simulations. *Nat. Methods* **2019**, *16* (8), 670−673.

https://doi.org/10.1021/acs.inorgchem.4c02299
Inorg. Chem. 2024, 63, 19074−19086